Plasma Sources Sci. Technol. **20** (2011) 024001 (15pp) doi:10.1088/0963-0252/20/2/024001

Particle simulation methods for studies of low-pressure plasma sources

Zoltán Donkó

Research Institute for Solid State Physics and Optics, Hungarian Academy of Sciences, H-1121 Budapest, Konkoly-Thege Miklós str. 29-33, Hungary

E-mail: donko@mail.kfki.hu

Received 30 August 2010, in final form 7 November 2010
Published 1 April 2011
Online at stacks.iop.org/PSST/20/024001

Abstract

This paper illustrates the application of particle simulation methods for the description of low-pressure discharges: Townsend discharges, cathode fall dominated dc glows and capacitively coupled radiofrequency discharges. The spatially and/or temporally varying electric field and the presence of boundaries (e.g. electrodes) in these plasma sources induce a non-hydrodynamic (or non-equilibrium) transport of some types of charged species, particularly of electrons. Particle-based methods provide, even under non-equilibrium conditions, a correct method of mathematical description of the particle transport and the determination of the distribution functions, which are crucial quantities in discharge modeling.

(Some figures in this article are in colour only in the electronic version)

1. Introduction

The understanding of the physics of gas discharges requires a precise mathematical description of the motion of charged particles. In many plasma sources of theoretical and practical interest the rapid spatial and/or temporal variation of the electrostatic or electromagnetic fields and the presence of boundaries (electrodes) induce *non-equilibrium* effects in the motion of these particles, especially of electrons [1]. A correct mathematical description under such conditions can only be expected from kinetic theory. As stated in a recent review by Tsendin [2]:

> '... Such a medium, called plasma by Langmuir, in each volume of which heavy particles at room temperature co-exist with electrons having energies larger by two orders of magnitude, is, obviously, extremely non-equilibrium and far from LTE. Therefore, the kinetic approach using a particle distribution function (first and foremost that of electrons) as the basic element is absolutely necessary for a plasma analysis.' (LTE = local thermodynamic equilibrium.)

In the kinetic approach the fundamental quantity describing the behavior of charged particles is the *velocity distribution function* (VDF) $f(\boldsymbol{r}, \boldsymbol{v}, t)$ that gives the probability distribution of particle velocity vectors at any spatial position ($\boldsymbol{r}$) and at any instance of time (t). In a plasma the distribution function evolves under the simultaneous influence of (i) any external fields and (ii) collisions of the particles. Mathematically, this evolution is described by the Boltzmann equation (BE):

$$\left[\frac{\partial}{\partial t} + \boldsymbol{a}\cdot\nabla_{\mathrm{v}} + \boldsymbol{v}\cdot\nabla_{\mathrm{r}}\right] f(\boldsymbol{r}, \boldsymbol{v}, t) = \left(\frac{\partial f}{\partial t}\right)_{\mathrm{coll}}. \qquad (1)$$

Here ∇_{v} and ∇_{r}, respectively, are gradients taken in velocity and real space, the term $(\partial f/\partial t)_{\mathrm{coll}}$ accounts for the effects of collisions. Several types of solution methods for the BE have been developed over recent decades and have been applied for the description of charged particle kinetics under swarm and discharge conditions [3]. The solution of the BE yields the VDF, from which the transport coefficients and collision (excitation, ionization, etc) rates—characterizing the macroscopic behavior of particle swarms—can readily be derived.

As an alternative to the solution of the BE, *particle simulation methods* also give access to the VDF and to all quantities derivable from that. This paper is devoted to briefly reviewing particle simulation methods and aims to illustrate how these methods aid the characterization of the behavior of charged particles in gas discharges. It is important to note that the two approaches, the solution of the BE and particle

simulations, are equivalent. Their relation is discussed in several works, see, e.g. [4, 5].

Particle-based simulations of gas discharges usually involve the Monte Carlo (MC) technique [6] to describe the interaction of charged particles with the background gas. Using the MC method a large number of particles are traced in the discharge within a specific domain of space and time, and the quantities of interest are obtained from accumulating information about the particles (e.g. the VDF can be 'built up' from the velocities of individual particles situated at (or 'near') a given spatial position at a given time). Particle simulations can be computationally demanding; nonetheless, these methods arose following the appearance of computers. The first MC simulations (of neutron transport) have been carried out on the MANIAC computer in the 1950s [7]. Thanks to the dramatic evolution of computer hardware, particle-based methods have continued to spread in all fields of plasma physics.

In this paper the application of particle simulation methods is illustrated for different types of low ionization degree plasmas. In section 2 the basics of the MC simulation—the method used in all the forthcoming examples—are explained in detail. In section 3 examples for the spatial and the spatio-temporal relaxation of electron swarms are given. In section 4 the role of particle simulation methods in the description of cold-cathode dc glow discharges is discussed. In section 5 we outline the basics of the particle-in-cell (PIC) simulation method, and apply it for the calculation of the spatial and temporal dependence of the characteristics of dual-frequency capacitive rf plasma sources. A short summary follows in section 6.

2. Monte Carlo simulation of electron transport

The task of describing the behavior of charged particles in the presence of external fields is twofold: one has to (i) follow the trajectories of the particles between collisions and (ii) handle the collisions of the particles with the background gas. (Here we consider only collisions of the traced particles with the atoms/molecules of the background gas, and neglect e.g. electron–electron collisions.)

The motion of particles between collisions is governed by the equation of motion:

$$m\ddot{\boldsymbol{r}} = q(\boldsymbol{E} + \boldsymbol{v} \times \boldsymbol{B}), \tag{2}$$

where q and m are, respectively, the charge and the mass of the particle, $\boldsymbol{E}$ is the electric field and $\boldsymbol{B}$ is the magnetic field. In the following we assume $\boldsymbol{B} = 0$. The trajectories of the particles can be obtained via the integration of the discretized form of (2) over Δt time steps. While the determination of particle trajectories this way between collisions is deterministic, collisions are treated in a stochastic (probabilistic) manner, that is what accounts for the name 'Monte Carlo simulation'. The approach relies on the generation of random numbers which, however, have specific probability distributions, based on physical principles.

In a rigorous treatment, all collision events have to be described in the *center of mass* (COM) frame. In the following $\boldsymbol{v}_1$ and $\boldsymbol{v}_2$ denote the velocity of the 'projectile', and the 'target' particles, respectively, in the laboratory (LAB) frame. m_1 and m_2 are the corresponding masses. In the following the steps of executing a collision in the simulation are outlined.

(1) Checking for the occurrence of a collision.
The probability for a collision to occur after a time interval Δt is given by

$$P(\Delta t) = 1 - \exp[-n\overline{\sigma_{\mathrm{T}}(v_{\mathrm{r}})v_{\mathrm{r}}}\Delta t], \tag{3}$$

where σ_{T} is the *total cross section* that includes the cross sections of all possible collision processes and $\boldsymbol{v}_{\mathrm{r}} = \boldsymbol{v}_1 - \boldsymbol{v}_2$ is the relative velocity of the collision partners. The average $\overline{\sigma_{\mathrm{T}} v_{\mathrm{r}}}$ has to be taken over the ensemble of target atoms of Maxwellian distribution (of temperature T_2) [4, 8]:

$$\overline{\sigma_{\mathrm{T}} v_{\mathrm{r}}} = \iiint \sigma_{\mathrm{T}}(|\boldsymbol{v}_1 - \boldsymbol{v}_2|)|\boldsymbol{v}_1 - \boldsymbol{v}_2| \left(\frac{m_2}{2\pi k T_2}\right)^{3/2} \times \exp\left(-\frac{m_2 v_2^2}{2kT_2}\right) \mathrm{d}v_{2x}\, \mathrm{d}v_{2y}\, \mathrm{d}v_{2z}. \tag{4}$$

The calculation of the collision probability (3) can significantly be simplified in the cases discussed later.

(2) Transformation of the particle velocities to the COM frame:

$$\boldsymbol{V}_1 = \boldsymbol{v}_1 - \boldsymbol{w}, \qquad \boldsymbol{V}_2 = \boldsymbol{v}_2 - \boldsymbol{w}, \tag{5}$$

where

$$\boldsymbol{w} = \frac{m_1\boldsymbol{v}_1 + m_2\boldsymbol{v}_2}{m_1 + m_2} \tag{6}$$

is the velocity of the COM, which does not change during the collision.

(3) Changing the *direction* and the *magnitude* of the relative velocity in accordance with the type of collision:

$$\boldsymbol{v}_{\mathrm{r}} \to \boldsymbol{v}'_{\mathrm{r}}. \tag{7}$$

(4) Calculation of the post-collision velocities in the laboratory frame:

$$\boldsymbol{v}'_1 = \frac{m_2}{m_1 + m_2}\boldsymbol{v}'_{\mathrm{r}} + \boldsymbol{w}, \qquad \boldsymbol{v}'_2 = -\frac{m_1}{m_1 + m_2}\boldsymbol{v}'_{\mathrm{r}} + \boldsymbol{w}. \tag{8}$$

In studies of electron transport it is customary to use the *cold gas approximation*, which assumes that the (background) gas atoms are at rest; $\boldsymbol{v}_2 = 0$. In this case $\boldsymbol{v}_{\mathrm{r}}$ becomes equal to the velocity of the electron, $\boldsymbol{v}_1$. Due to the large mass ratio between atoms and electrons, executing the collision in the laboratory frame represents a good approximation, as long as the mean electron energy is much higher than the thermal energy of the gas atoms. The opposite occurs only at very low values of the reduced electric field—under such conditions executing the collision in the COM frame is the proper procedure to follow, see, e.g. [9].

In the limit of the cold gas approximation ($\boldsymbol{v}_2 = 0$ and thus $\boldsymbol{v}_{\mathrm{r}} = \boldsymbol{v}_1$) the probability of a collision during a time step Δt becomes

$$P(\Delta t) = 1 - \exp[-n\sigma_{\mathrm{T}}(v_1)v_1\Delta t]. \tag{9}$$

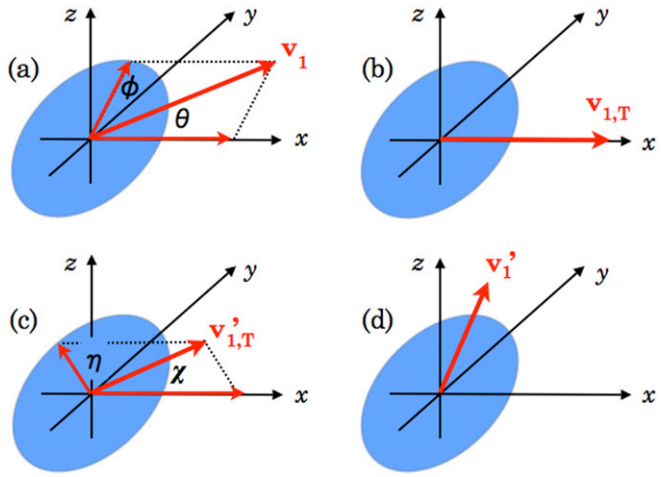

Figure 1. Steps of changing the velocity of the projectile in an electron–atom collision. (The angles θ and χ are measured from the x-axis, while ϕ and η lie in the (y, z) plane.)

Carrying out the collision in the LAB frame is fully justified under the conditions of interest here. The steps of changing the electron's velocity are discussed below and are illustrated in figure 1. First we have to find the angles θ and ϕ that define the Cartesian components of the velocity vector $\boldsymbol{v}_1$ before the collision (see figure 1(a)):

$$\boldsymbol{v}_1 = \begin{bmatrix} v_x \\ v_y \\ v_z \end{bmatrix} = v_1 \begin{bmatrix} \cos\theta \\ \sin\theta\cos\phi \\ \sin\theta\sin\phi \end{bmatrix}. \tag{10}$$

As the next step we transform $\boldsymbol{v}_1$ to point into the x direction (see figure 1(b)); this is done by two rotations of the velocity vector: (i) by an angle $-\phi$ around the x-axis and (ii) by an angle $-\theta$ around the z-axis. Let us denote the matrices describing these operations by $\boldsymbol{T}_x(-\phi)$ and $\boldsymbol{T}_z(-\theta)$. The transformed velocity vector is thus

$$\boldsymbol{v}_{1,\mathrm{T}} = \boldsymbol{T}_z(-\theta)\boldsymbol{T}_x(-\phi)\boldsymbol{v}_1 = v_1 \begin{bmatrix} 1 \\ 0 \\ 0 \end{bmatrix}. \tag{11}$$

Actually, the $\boldsymbol{T}_z(-\theta)\boldsymbol{T}_x(-\phi)\boldsymbol{v}_1$ product does not need to be calculated here as we know that $\boldsymbol{v}_{1,\mathrm{T}}$ will point into the x direction. The inverse of this transformation, however, will be needed later on.

The deflection and the change in the magnitude of the velocity vector is defined by the type of collision. The type of process to take place is chosen randomly, according to the cross sections of the individual possible processes, at the given energy, ε, of the colliding electron. The probability of process k (having a cross section $\sigma_k(\varepsilon)$) is

$$P_k = \frac{\sigma_k(\varepsilon)}{\sigma_{\mathrm{T}}(\varepsilon)}. \tag{12}$$

Let us first describe the deflection of the direction during a collision. The collision is characterized by two angles: the scattering angle χ and the azimuth angle η. In cases when the differential cross section $\sigma(\varepsilon, \chi)$ is known (from experiment or from a model [10]), χ is found from

$$\frac{\int_0^{\chi} \sigma(\varepsilon, \chi')\sin\chi' \mathrm{d}\chi'}{\int_0^{\pi} \sigma(\varepsilon, \chi')\sin\chi' \mathrm{d}\chi'} = R_{01}, \tag{13}$$

otherwise, to have an isotropic scattering, it can be set to

$$\chi = \arccos(1 - 2R_{01}). \tag{14}$$

Here (and in the following) R_{01} denotes a random number uniformly distributed over the [0,1) interval. The azimuth angle is usually chosen as

$$\eta = 2\pi R_{01}. \tag{15}$$

In ionization processes the generation of a second set of the two angles (for the ejected electron) is based on the assumption that the velocity vectors of the incoming, the scattered and ejected electrons lie in the same plane.

Next, the magnitude of the velocity vector is changed according to the type of process. For elastic scattering the (relative) energy loss is

$$\frac{\Delta\varepsilon}{\varepsilon} = -\frac{2m_1m_2}{(m_1+m_2)^2}(1-\cos\chi) \overset{m_1 \ll m_2}{\longrightarrow} -2\frac{m_1}{m_2}(1-\cos\chi). \tag{16}$$

In the case of an excitation process

$$\Delta\varepsilon = -\varepsilon_j, \tag{17}$$

where ε_j is the energy level associated with the excitation process j, and finally, in the case of ionization the scattered and ejected electrons share the remaining energy:

$$\varepsilon_{\mathrm{scatt}} + \varepsilon_{\mathrm{eject}} = \varepsilon - \varepsilon_{\mathrm{ion}}. \tag{18}$$

In the latter process the partitioning of the energy between the scattered and ejected electrons can be assigned randomly or can be based on experimental data [11]:

$$\varepsilon_{\mathrm{eject}} = \bar{E}\tan\left[R_{01}\arctan\left(\frac{\varepsilon - \varepsilon_{\mathrm{ion}}}{2\bar{E}}\right)\right], \tag{19}$$

where $\bar{E}$ is a characteristic parameter of the gas.

Having generated the scattering and azimuth angles, and having as well changed the magnitude of the velocity ($v_1 \to v_1'$) due to the energy change, the velocity vector is deflected, as shown in figure 1(c):

$$\boldsymbol{v}_{1,\mathrm{T}}' = v_1' \begin{bmatrix} \cos\chi \\ \sin\chi\cos\eta \\ \sin\chi\sin\eta \end{bmatrix}, \tag{20}$$

and is subsequently transformed back to the original coordinate system by the inverse rotation operations (see figure 1(d)):

$$\begin{aligned} \boldsymbol{v}_1' &= \boldsymbol{T}_x(\phi)\boldsymbol{T}_z(\theta)\boldsymbol{v}_{1,\mathrm{T}}' \\ &= v_1' \begin{bmatrix} \cos\theta & -\sin\theta & 0 \\ \sin\theta\cos\phi & \cos\theta\cos\phi & -\sin\phi \\ \sin\theta\sin\phi & \cos\theta\sin\phi & \cos\phi \end{bmatrix} \begin{bmatrix} \cos\chi \\ \sin\chi\cos\eta \\ \sin\chi\sin\eta \end{bmatrix}, \end{aligned} \tag{21}$$

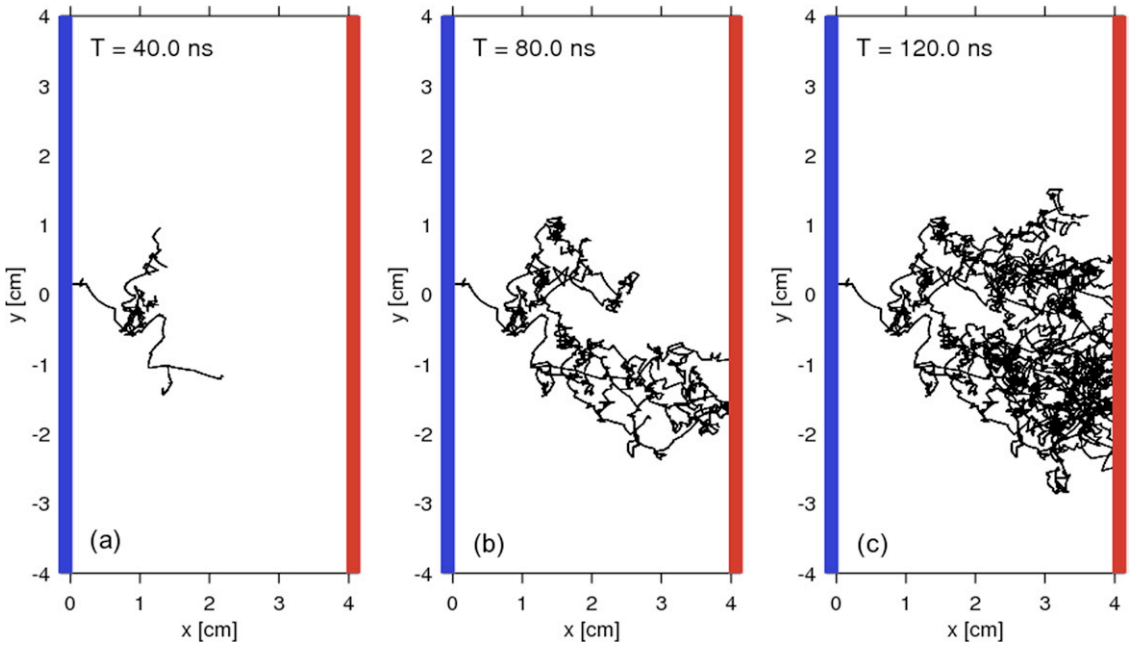

Figure 2. Snapshots of an MC simulation of the development of an electron avalanche in a Townsend discharge in argon, at $p = 41.4$ Pa and $E/N = 500$ Td. The cathode is situated at $x = 0$, while the anode is at $x = 4$ cm. A movie of the development of the avalanche is accessible online [14].

which gives the final result for the post-collision velocity vector as

$$\boldsymbol{v}_1' = v_1' \times \begin{bmatrix} \cos\theta\cos\chi - \sin\theta\sin\chi\cos\eta \\ \sin\theta\cos\phi\cos\chi + \cos\theta\cos\phi\sin\chi\cos\eta - \sin\phi\sin\chi\sin\eta \\ \sin\theta\sin\phi\cos\chi + \cos\theta\sin\phi\sin\chi\cos\eta + \cos\phi\sin\chi\sin\eta \end{bmatrix}. \quad (22)$$

The simplest MC simulation approach is based on (i) advancing the particle according to the equation of motion for a time Δt (updating its position and velocity vectors) and (ii) checking for the occurrence of a collision using equation (9). In practice, one has to choose Δt to be small enough to allow an accurate integration of the equation of motion and to keep the probability of more than one collision to occur during the time step at a negligible value.

After implementing the procedures described above into a code, we are ready to trace the electrons' motion under the effect of an external electric field, as in a Townsend discharge. We take as an example an argon discharge formed within a gap of $L = 4$ cm, between plane and parallel electrodes, at a reduced electric field of $E/n = 500$ Td ($1\,\text{Td} = 10^{-21}\,\text{V m}^2$). Under such conditions a significant multiplication of the electrons takes place and, initiated by the emission of electrons from the cathode, *electron avalanches* build up. In the MC code the following approach is used to trace avalanches: (1) the simulation starts with emitting a single electron from the cathode; (2) the electron is traced until it reaches the anode; meanwhile, the initial parameters (position and velocity coordinates) of electrons created in ionization events are stored in a 'stack'; (3) if the stack is not empty, the electron at the top of the stack is assigned to be the next to be traced; (4) steps 2–3 are carried out repeatedly until the stack becomes empty. Displaying the trajectories up to given values of time, the temporal development of an electron avalanche can be visualized, as shown in figure 2. The collision cross sections have been taken from [12].

It is noted that, although this setting represents the simplest possible electrode configuration, even here the presence of boundaries induces a non-equilibrium behavior and limits the validity of a hydrodynamic approach. Thus, correct results for this, and similar problems can be expected only from a kinetic approach.

The basic MC simulation procedure can be improved in several ways. Calculating the collision probability for a high number of simulation particles in each time step Δt may become computationally demanding. The so-called *null-collison method* [13] can accelerate simulations considerably. The basic idea of the approach is to add a fictitious process to the set of real elementary collision processes, thereby ensuring that the *total collision frequency*

$$\nu^* = \max\{n\sigma_T(v_1)v_1\} \quad (23)$$

becomes independent of the particle velocity. This way a time of free flight until the next collision

$$\tau = -\frac{1}{\nu^*}\ln(1 - R_{01}) \quad (24)$$

can be assigned to a given particle. In an MC simulation the trajectory of this particle can be integrated for this time interval, without the need for checking for the occurrence of a collision after each time step Δt, which speeds up the computations, as normally $\tau \gg \Delta t$. After the free flight (when the electron has a velocity v_1) a real collision occurs with a probability

$$P_{\text{real}} = \frac{\nu_{\text{real}}}{\nu^*} = \frac{n\sigma_T(v_1)v_1}{\nu^*}, \quad (25)$$

otherwise the particle proceeds (without any change in its velocity vector) along its trajectory for a next free flight. Whenever a real collision occurs, it is handled in the same way as it has been described above.

Using the null-collision method one can avoid the calculation of the collision probability (3) if the motion of the background gas atoms must not be neglected, which is the typical case for ions [15]. Using an upper bound for the total collision frequency with a reasonable limit for the highest possible *relative* velocity, one can assign a flight time for ions as given by (24). Upon a check for a collision, one can choose a collision partner (with a velocity vector $\boldsymbol{v}_2$) from the background gas atoms having a Maxwellian distribution, and calculate the probability of a real collision as

$$P_{\mathrm{real}} = \frac{\nu_{\mathrm{real}}}{\nu^*} = \frac{n\sigma_{\mathrm{T,ion}}(|\boldsymbol{v}_1 - \boldsymbol{v}_2|)|\boldsymbol{v}_1 - \boldsymbol{v}_2|}{\nu^*}. \qquad (26)$$

We end this section by noting that collision processes not mentioned above, such as superelastic collisions and attachment processes can also be incorporated in the MC scheme, as well as Coulomb (electron–electron) collisions [16]. Processes occurring at the boundaries (reflection, absorption, etc) can also be accounted for in a straightforward way. At very high ionization or attachment rates, re-scaling procedures may need to be applied [17] to keep a reasonable number of particles in the simulation.

3. Electron kinetics in a homogeneous electric field

Particle simulations have been aiding *swarm* studies concerning both electrons and ions in background gases. In these calculations low charge densities are assumed and interactions between the charged particles are usually neglected. Based on the collision cross sections swarm calculations yield the distribution function of the particles, as well as their transport coefficients, which are important data for the modeling of gas discharges. Moreover, as some of the transport coefficients can be measured in experiments, swarm calculations also aid the validation and adjustment of cross section sets [18].

The settings we consider here are one-dimensional in space (swarm and discharge characteristics change over one spatial coordinate) but the particles move in 3D space with three position and three velocity coordinates. This symmetry reduces the VDF to depend on one spatial coordinate and on the axial and radial velocity only, i.e. $f(\boldsymbol{r}, \boldsymbol{v}, t) = f(x, v_x, v_\mathrm{r}, t)$. We investigate the transport of electrons in argon gas, the e^- + Ar cross sections are taken from [12].

The evolution of swarm transport parameters and the electron VDF in an argon steady state Townsend discharge (f becomes independent of t as well) at a reduced electric field of $E/n = 500\,\mathrm{Td}$ and at a discharge gap $L = 1\,\mathrm{cm}$ is considered first. Electrons are emitted from the cathode with an energy of 1 eV into directions randomly distributed over a half sphere. The anode is assumed to be perfectly absorbing. To obtain good statistics the number of primary electrons was chosen to be 5×10^5, which resulted in a total number of collisions of several hundred million. Figures 3(*a*)–(*c*) show the spatial evolution of the transport parameters derived from this simulation: the mean energy $\langle\varepsilon\rangle$, the drift velocity v_{dr}, and the Townsend ionization coefficient α. The latter is calculated from the spatial growth of the electron flux, ϕ_e, as $\alpha(x) = \mathrm{d}\phi_\mathrm{e}(x)/[\phi_\mathrm{e}(x)\mathrm{d}x]$. The VDFs of the electrons, $f(v_x, v_\mathrm{r})$, at selected spatial coordinates are plotted in figures 3(*d*)–(*k*). Here v_x and v_r, respectively, are the velocity components parallel with and perpendicular to the direction of the electric field.

In figures 3(*a*)–(*c*) we can identify three characteristic regions, although the electric field is homogeneous in the whole gap. Near the cathode the swarm is not in equilibrium with the electric field, along the 'equilibration length' [19]—characteristic for the gas and the reduced electric field—the transport parameters change significantly even though the electric field is homogeneous. The analysis of the VDFs in this region, $x/L \lesssim 0.4$, shows significant changes as well. At $x/L = 0.05$ the swarm is still monoenergetic, but its VDF already became isotropized due to elastic collisions; this shows up in figure 3(*d*) as a VDF consisting of a circle. Drifting away from the cathode and having reached an energy for excitation and ionization the shape of the VDF changes to be composed of concentric rings, which correspond to groups of electrons that have undergone a different number of inelastic collisions. This structure gradually smears out as the swarm reaches equilibrium at around $x/L \approx 0.4$.

Beyond this point in space the transport parameters acquire their equilibrium values whilst the electron density and the electron flux in this region ($0.4 \leqslant x/L \leqslant 0.9$ in our case) increase exponentially. The distortion of the VDF due to the drift is clearly visible in panels (*i*) and (*j*) of figure 3.

The third characteristic feature in the behavior of the transport parameters is caused by the absorbing boundary. Near the anode we observe an increase in the mean energy and of the drift velocity, and a decrease in the ionization coefficient. This behavior of the transport parameters, which may look counterintuitive from first sight, can be explained by the complex, non-trivial behavior of the VDF near the surface. The density of electrons located in certain regions of the velocity space is depleted, in particular, the electron population propagating into the negative x direction, as can be seen in figure 3(*k*). Due to this asymmetry of the VDF the drift velocity increases by almost a factor of three near the anode. (In reality a fraction of the electrons may be reflected from the electrode, thus, this effect is expected to be less pronounced in a real discharge.) The strong depletion of the population of slow electrons (compare panels (*j*) and (*k*) of figure 3) results in an increase in $\langle\varepsilon\rangle$, whereas the lower number of high energy electrons (with $v > 2.35 \times 10^6\,\mathrm{m\,s^{-1}}$, corresponding to the ionization threshold of argon) with $v_x < 0$ results in a decrease in α.

As a second example, we analyze a time-dependent problem: we investigate the spatio-temporal relaxation of the electron gas in a finite volume, as it has been done in a combined BE-MC calculation study in [20]. Electrons are released with a steady flux at $x = 0$ with isotropically

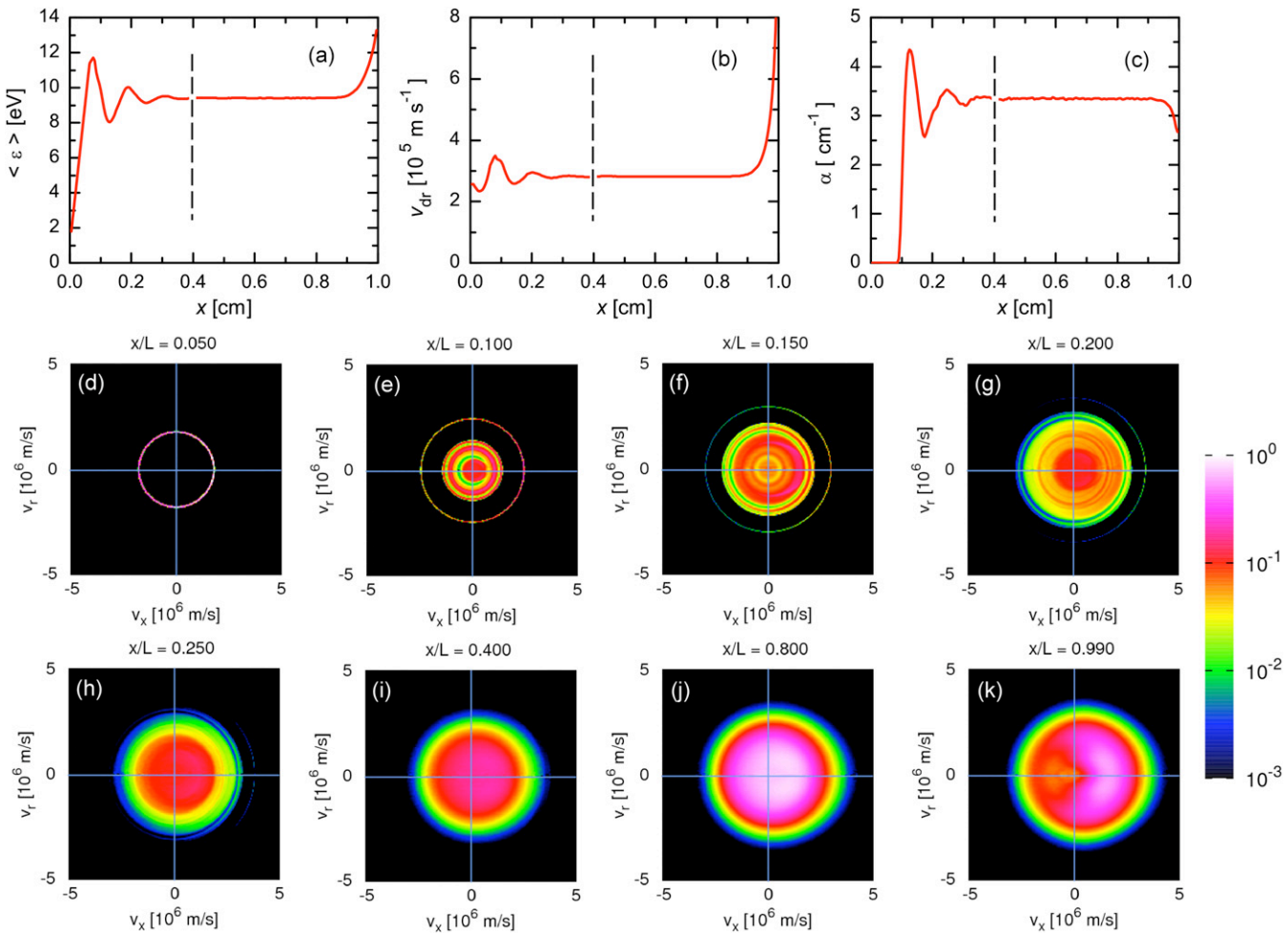

Figure 3. Transport parameters of an electron swarm in argon gas at $E/n = 500$ Td and an electrode gap $L = 1$ cm: (*a*) mean energy, (*b*) drift velocity, and (*c*) Townsend ionization coefficient. The vertical dashed lines indicate the end of the equilibration region. (*d*)–(*k*) illustrate VDFs of electrons at selected spatial positions. The color scale of the VDFs is logarithmic and covers three orders of magnitude.

distributed initial direction and a Gaussian energy distribution with a mean energy of 5 eV and a width of 2 eV. The anode, which is perfectly absorbing, is situated at $L = 10$ cm. The electric field is set to $E = 2\,\mathrm{V\,cm^{-1}}$. This value is changed at $t = 0$ to $E = 6\,\mathrm{V\,cm^{-1}}$. The gas pressure is 133 Pa and the gas temperature is $T = 273$ K. Under these conditions the reduced electric fields corresponding to the above values are 6.4 Td and 19.2 Td, respectively.

The panels of figure 4 show the distribution functions $f(\varepsilon)/\sqrt{\varepsilon}$ in the form of color maps, over the space–energy plane. The stationary distribution at $t < 0$ is depicted in panel (*a*). At $E/n = 6.4$ Td the energy loss of the electrons is mainly due to elastic collisions; consequently no pronounced spatial structures appear. Following the instantaneous increase in the electric field, patterns specific to periodic energy gain (from the field) and loss (due to inelastic collisions) of the drifting electrons appear at the cathode side. These patterns fill up the whole gap as time passes, as seen in panels (*b*)–(*h*) of figure 4. The 'new' stationary state (resembling the features of the Franck–Hertz experiment) is formed after about 10 μs.

4. Particle simulation in modeling of cold-cathode glow discharges

In this section we go beyond the simulation of electron swarms and attempt a mathematical description of cold-cathode dc glow discharges, where appreciable space charge is present in the cathode region [21]. The 'cathode region' of these discharges is of primary interest as the processes responsible for self-sustainment take place in this part of the discharge, via gas-phase and surface reproduction of charges. The cathode sheath and the negative glow parts—belonging to the cathode region, and adjacent to each other—exhibit very different characteristics. The sheath region is characterized by a high and spatially changing electric field (and a voltage drop, the 'cathode fall', which typically amounts to several hundred volts). The negative glow is characterized by a nearly quasi-neutral plasma and a low electric field. The length of the sheath is typically comparable to the energy relaxation length and the ionization mean free path of the electrons. Under such highly non-equilibrium conditions [1] an accurate description of the electrons' motion is a real challenge for theoretical approaches.

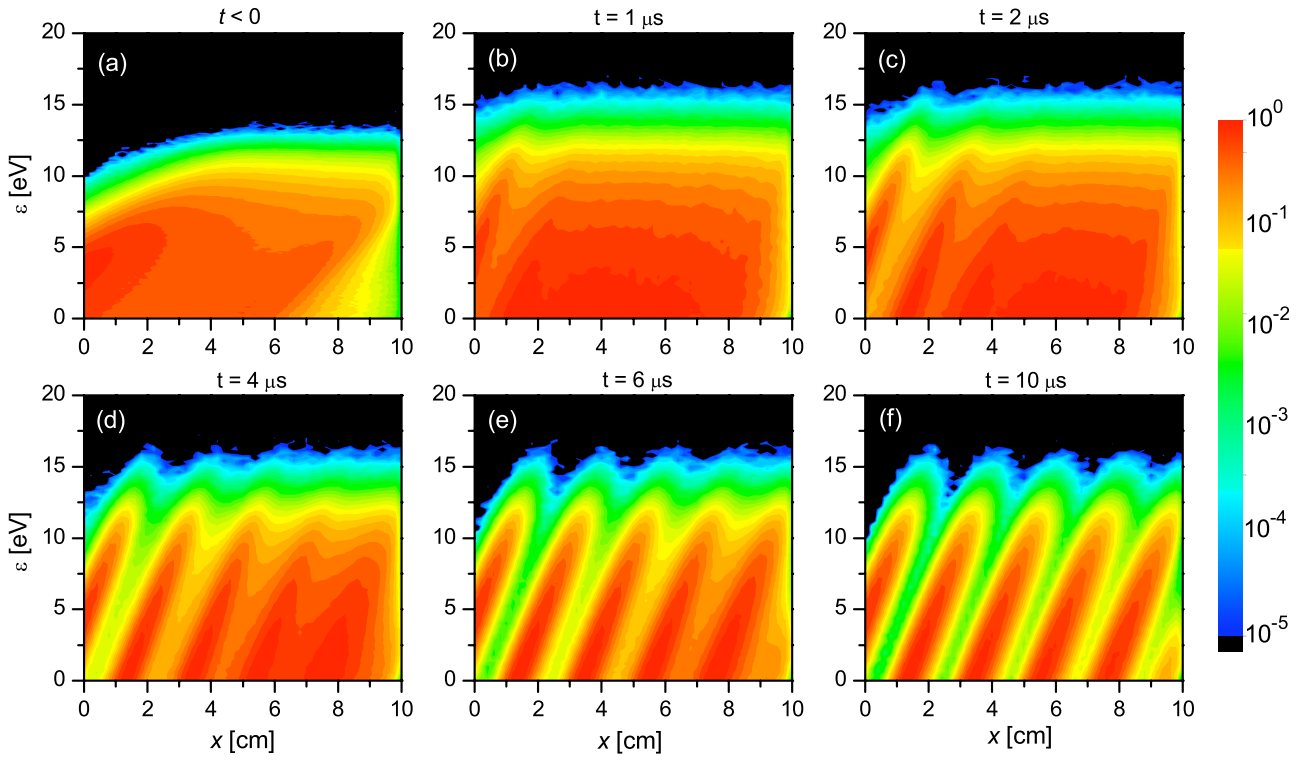

Figure 4. Color map representation of the distribution function $f(\varepsilon)/\sqrt{\varepsilon}$ of the electrons at selected times during the spatio-temporal relaxation of the electron swarm. The color scale is logarithmic and spans five orders of magnitude down from the maximum value of each data set. Here $p = 133$ Pa (argon), $T = 273$ K. $E = 2\,\mathrm{V\,cm^{-1}}$ at $t < 0$ and $E = 6\,\mathrm{V\,cm^{-1}}$ at $t \geqslant 0$. Electrons are emitted isotropically at $x = 0$ cm. Data reproduced from [20], Loffhagen D *et al* 2002 *Eur. Phys. J. Appl. Phys.* **18** 189, Copyright EDP Sciences, http://www.epjap.org/

For a self-consistent characterization of the discharge, in addition to the description of the motion of the electrons, ions have to be dealt with as well, and the Poisson equation has to be used to calculate the electric field. For the ions the assumption of hydrodynamic (local-field) approximation is reasonable in most dc noble gas discharges. In such an approach ions are treated as a continuum.

In *fluid* models all the plasma species, including electrons, are treated as continuum. Fluid models are based on a truncated set of moment equations of the BE. 'Simple' fluid models consider the first two moments (expressing particle and momentum conservation) by including a pair of continuity equations and a pair of momentum balance equations, for electrons and ions, as well as the Poisson equation. The non-local (non-equilibrium) transport of electrons can to some extent be incorporated in 'extended' fluid models (see the discussion in [22]) by including an additional equation for the electron mean energy (the third moment of the BE) in the calculations. In the latter class of models a kinetic swarm (BE or MC) calculation is carried out (prior to running the discharge simulation code) to establish the relations between the electron mean energy and the diffusion and mobility transport coefficients of the electrons and of the electron energy, as well as the relevant reaction (e.g. ionization) and energy loss rates. These relations are subsequently used when running the fluid code (see, e.g. [23]).

The advantages of fluid models (efficiency) and of particle treatment (accuracy) can be jointly utilized in *hybrid* models [24], in which slow plasma species are treated within the frame of a fluid model, while fast species (in particular fast electrons, which drive ionization and excitation reactions) are treated as particles. This approach avoids the need for the MC simulation of the whole electron population, which may be problematic for the slow trapped electrons accumulating in the negative glow due to the field reversal [25]. Previous studies have indeed shown that the importance of the kinetic treatment of electrons in the dc cathode region lies in the possibility of obtaining an accurate ionization source function [26]. Although one needs to be aware of their limitations [27], hybrid models have been quite successful in describing a wide range of discharge physics phenomena and in providing deep insight into the operation of different sources [28].

In the following—based on the work of Derzsi *et al* [26]—we shall compare representative discharge characteristics calculated by the three different types of models mentioned above: the simple and extended fluid models, as well as a hybrid model. Here, we are limited to describe the models only concisely; the reader is referred to [26] for more details.

In the case of fluid models the calculation of the ionization source function can be based both on the electron flux or the electron density [29]. In simple fluid models the 'flux-based source' calculation uses Townsend's first ionization coefficient α, as a function of the *local* reduced electric field:

$$S(x) = \alpha[E(x)/n]|\phi_e(x)|, \tag{27}$$

where ϕ_e is the electron flux and n is the gas density. In the extended fluid model α as a function of the *electron mean*

energy $\bar{\varepsilon}$ is used and the source function is calculated as

$$S(x) = \alpha[\bar{\varepsilon}(x)]|\phi_e(x)|. \quad (28)$$

The approach, based on the electron density, n_e, uses a rate coefficient k_i, which depends on the electron mean energy:

$$S(x) = k_i[\bar{\varepsilon}(x)]n_e(x)N. \quad (29)$$

This expression is called here a 'rate coefficient-based source' calculation. The accurate approach to obtain the rate coefficient is based on a kinetic swarm calculation mentioned above. As stated in [29], the flux-based calculation of the source function is expected to be more accurate in the cathode region of glow discharges than the rate coefficient-based calculation, as the accuracy of the calculated electron flux is usually much higher than the accuracy of the calculated density (see also the findings of [27]). In the case of the hybrid model electrons are traced by an MC simulation in the electric field distribution obtained in the fluid module. After completing the MC simulation cycle of a given number of primary electrons and of the electrons created by them in ionizing collisions, the source functions of ions and slow electrons (in a one-dimensional model) are obtained as

$$S_{i,e}(x) = \frac{j}{e(1+1/\gamma)\Delta x}\frac{N_{i,e}(x)}{N_0^{MC}}, \quad (30)$$

where j is the current density calculated in the previous fluid cycle, γ is the electron emission coefficient of the cathode and $N_{i,e}(x)$ is the number of ions (slow electrons) created in the slab of width Δx around x due to the emission of N_0^{MC} primary electrons from the cathode [24].

With regard to transport coefficients, for positive ions a mobility coefficient μ_i depending on the reduced electric field E/N, and known from experiments, is usually used in fluid and hybrid models. The diffusion coefficient of positive ions is in many cases taken as $D_i/\mu_i = ekT_i$, where k is the Boltzmann constant and kT_i is the characteristic energy of ions (T_i is usually assumed to be equal to the gas temperature T_g). For electrons, in simple fluid models and in most hybrid models, constant values are used for μ_e and D_e. The mobility coefficient usually has an experimental value, and constant characteristic energy values between $kT_e = 0.1$ eV and 1 eV are routinely used to obtain the diffusion coefficient D_e, via the relation $D_e/\mu_e = ekT_e$. The effect of the assumed value of the characteristic energy of bulk electrons, kT_e, has been analyzed in e.g. [27]. It has been shown that some of the calculated discharge characteristics (particle densities and the depth of the potential well formed in the negative glow) depend sensitively on the assumed value of kT_e, while some other characteristics (particle fluxes and the voltage-current characteristics of the discharge) are basically independent of this value. As for electrons, calculating the transport coefficients based on the local mean electron energy was found to be superior to the calculation based on the local electric field [30]. In addition, numerical instabilities were observed when electron transport coefficients, which were functions of the local electric field strength, were used in 'simple' fluid models.

Figure 5 shows some of the discharge characteristics obtained using the different modeling approaches, for a set of reference conditions: $p = 40$ Pa (argon), $V = 441$ V, $T_g = 300$ K, $L = 3$ cm, $\gamma = 0.033$. The results of the simple fluid and hybrid models are shown for bulk electron temperature values $kT_e = 0.1$ eV and 1 eV, as well as a 0.28 eV value determined by Langmuir probe measurements for this set of discharge conditions [26]. As stated earlier, the transport coefficients of the electrons and electron energy—used in the extended fluid model—have been obtained as a function of mean energy, via MC swarm simulations. Figure 5(*a*) compares the electric field distributions resulting from the different models. The extended fluid model and the hybrid model predict a reversal of the electric field in the negative glow region [25, 31]. The simple fluid model cannot account for the field reversal, as it does not capture the non-local character of electron transport to any extent. The hybrid model results in a significantly shorter cathode sheath length (and consequently, an approximately factor of two stronger electric field at the cathode), compared with the fluid models, due to the enhanced ionization rate.

The calculated electron density distributions are plotted in figure 5(*b*). The peak of the electron density obtained from the different fluid models scatters approximately between 10^6 cm^{-3} and 5×10^7 cm^{-3}. The hybrid models, in contrast to these values, predict densities in the range 3×10^{10}–2×10^{11} cm^{-3}, depending on the bulk electron temperature assumed. Using the experimentally determined, $kT_e = 0.28$ eV, the hybrid model gives an electron density value consistent with the experiment. Similar agreement was found earlier in studies of a helium glow discharge [32].

The ionization source functions are compared in figure 5(*c*). The different fluid models predict quite different magnitudes and shapes for $S(x)$. It is only the hybrid model, which traces the fast electrons by MC simulation, that produces an exponential fall-off of the ionization source term past the sheath–glow boundary. As the ionization and excitation cross sections have similar forms and both processes are primarily driven by fast electrons (of which the energy may exceed by far the thresholds of these processes), it is reasonable to assume that the spatial distribution of the excitation rate exhibits the same behavior as the ionization rate. The light intensity in the negative glow is known to decrease exponentially, see, e.g. [33]; such behavior is predicted by the hybrid model only, in sharp contrast with the fluid models.

It is to be emphasized that the success of the hybrid approach is due to its ability to provide an accurate ionization source function under the highly non-local character of the cathode region. This latter is further illustrated in figure 6. The electric field profile shown in figure 6(*a*) is taken from the hybrid simulation. The ionization coefficient $\alpha(x)$ (which is a result of the MC simulation part of the hybrid model), seen in figure 6(*b*) is clearly not in equilibrium with the field. Within the sheath it shows an increasing tendency while the electric field decreases, and beyond the sheath–glow boundary (at around $x = 0.6$ cm) α decays quite slowly, whereas the electric field becomes very small. The flux of electrons (right scale of figure 6(*b*)) grows to more than double beyond the

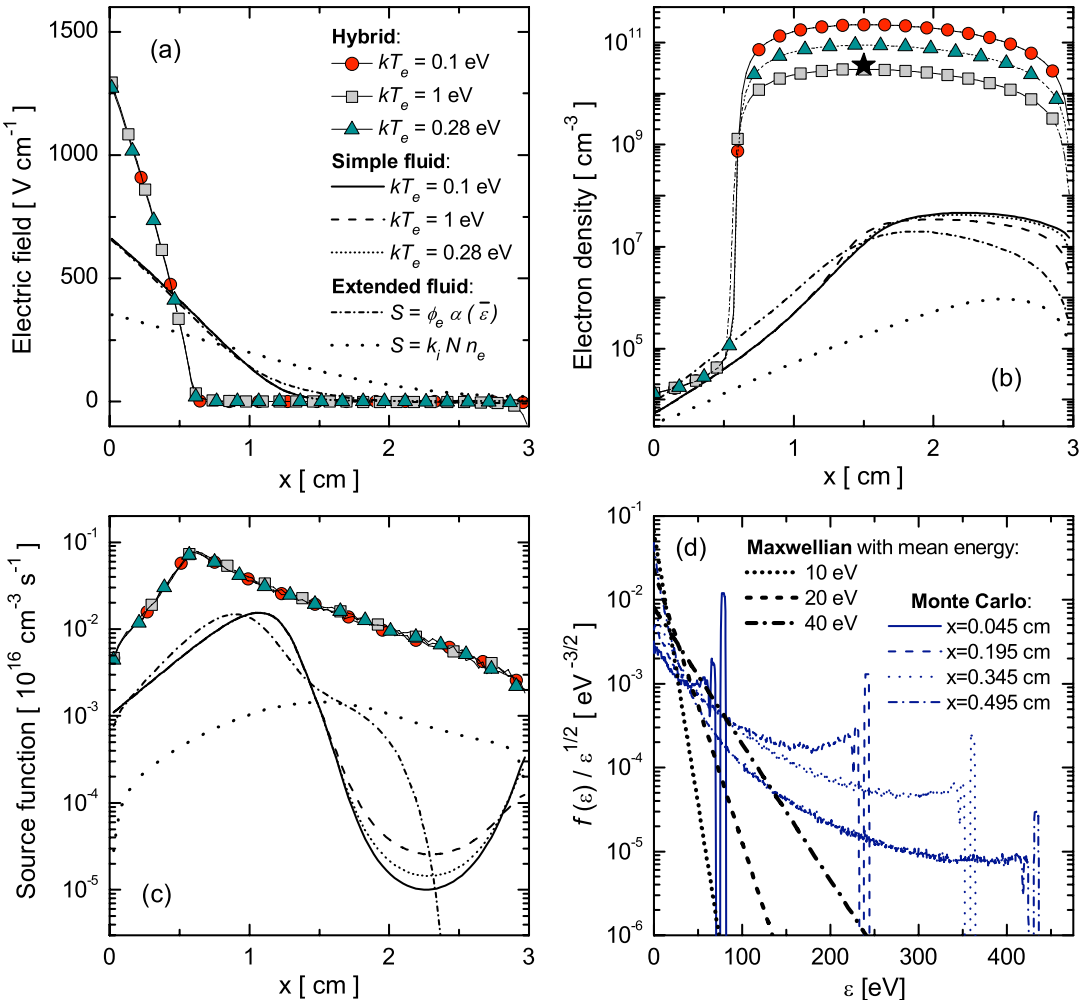

Figure 5. Results obtained by the different modeling approaches for a dc argon discharge at $p = 40$ Pa, $V = 441$ V, $T_g = 300$ K, $L = 3$ cm, $\gamma = 0.033$. (*a*) Electric field distributions, (*b*) electron density distributions and (*c*) ionization source functions. The symbol $\star$ in (*b*) shows the density determined by Langmuir probe measurement [26]. The legend shown in (*a*) applies to panels (*b*) and (*c*), as well. (*d*) The distribution function of electrons at several places in the cathode sheath and Maxwellian distribution functions with specified mean energy values. Panels (*a*)–(*c*) reproduced from [26] Derzsi A *et al* 2009 *J. Phys. D: Appl. Phys.* **42** 225204, Copyright IOP Publishing Ltd.

sheath–glow boundary, indicating a significant ionization by the fast electrons streaming into the glow from the sheath. The VDFs of electrons at several positions between the cathode and the sheath–glow boundary are plotted in panels (*c*)–(*h*) of figure 6. The VDFs are very anisotropic, especially near the cathode, due to the high field. The beam component of the electron stream (having not suffered any inelastic energy losses) is visible up to the sheath–glow boundary. From the shapes of the VDFs it is clear that any BE approaches have to use a high number of terms to describe the electrons' passage through the cathode fall. It is also clear that the VDFs are very far from Maxwellian distributions, as already pointed out in previous works, e.g., in the pioneering studies of [34], where the evolution of the electron energy distribution function in the sheath of a helium glow discharge has been investigated.

5. PIC simulation of radiofrequency discharges

As the last topic of this paper we discuss the PIC method, which represents the most widespread simulation technique for the kinetic description of radiofrequency (rf) plasma sources. The method, which belongs to the class of 'particle-mesh' approaches, was introduced in the 1960s and has developed significantly during the following decades [35, 36]. The idea of using a computational mesh avoids the need to account for the pairwise interaction of all individual particles. The other idea, to use 'superparticles', which represent a large number of real particles, brings the number of particles in the simulation into a tractable order of magnitude. While the PIC scheme can account for electromagnetic effects [37], here we restrict ourselves to electrostatic simulations.

In simulations of low-pressure discharges the collisions are usually treated by an MC method. The simulation scheme resulting from this combination of the techniques is referred to as the PIC/MCC approach [38] (MCC = Monte Carlo collisions). For *bounded* and *collisional* plasmas of interest here, the PIC/MCC simulation cycle consists of the following steps [38–41], which are also shown in figure 7:

(i) at each time step the charge of the superparticles (which can be situated at any position inside the discharge gap) is assigned to a grid;

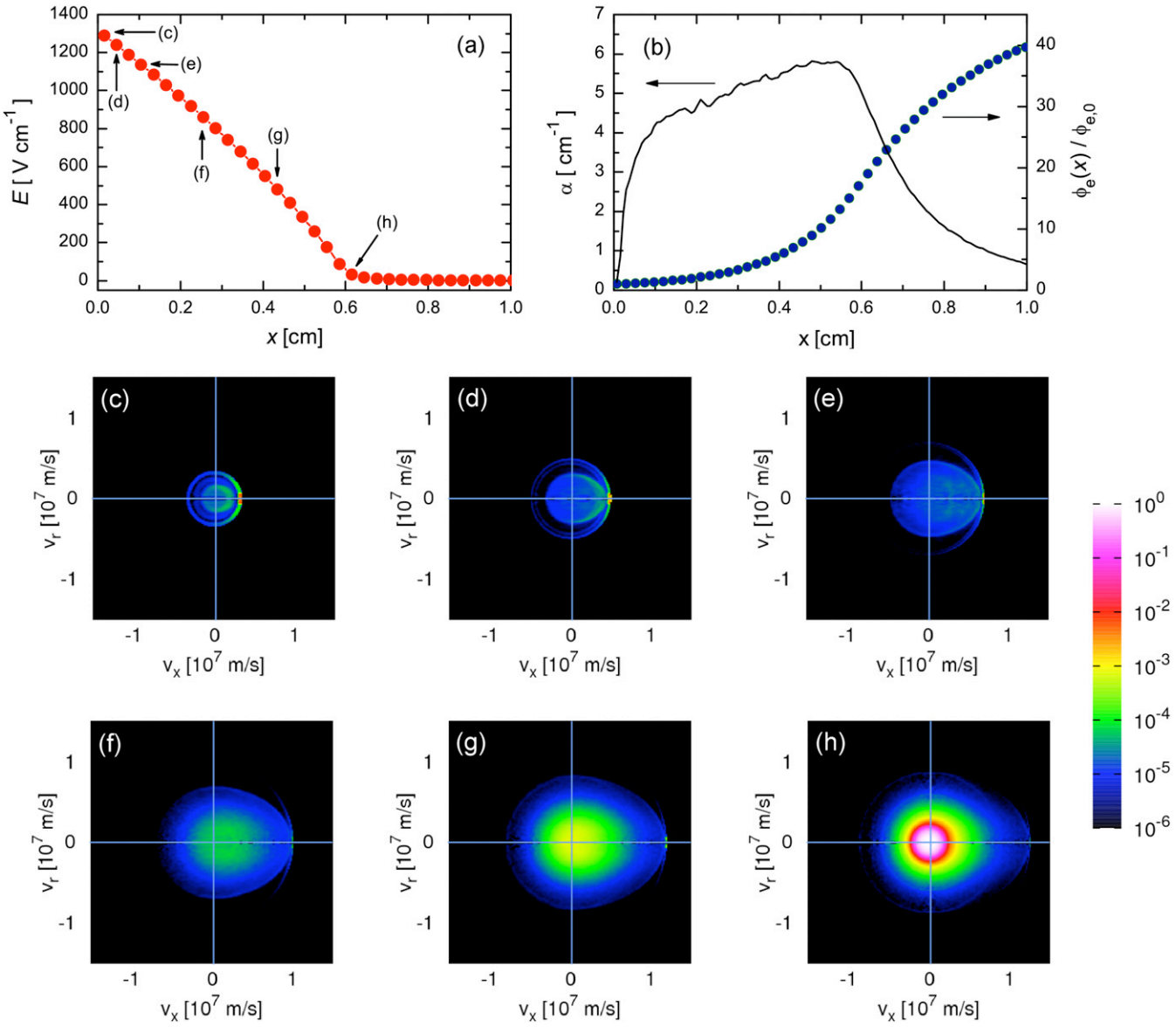

Figure 6. Discharge characteristics as obtained from the hybrid model for the same discharge conditions as in figure 5. (*a*) Electric field distribution, (*b*) ionization coefficient α and electron flux normalized to its value at the cathode $\phi_e/\phi_{e,0}$. (*c*)–(*h*) Electron VDFs at selected positions in the cathode sheath (indicated in (*a*)). The color scale of the VDFs is logarithmic and covers six orders of magnitude. Note the pronounced anisotropy of the VDFs.

(ii) the Poisson equation is solved on the grid: the potential distribution is calculated from the charge distribution, taking into account the potentials applied (or the current driven) to the electrodes, as boundary conditions;

(iii) the forces acting on the particles are obtained by interpolation of the electric field (resulting from the differentiation of the potential) to the positions of the particles;

(iv) the new positions and velocities of the particles are obtained from the solution of the equation of motion;

(v) due to the finite volume of the plasma the interaction of the particles with the surrounding surfaces (e.g. reflection, absorption, secondary emission) is accounted for;

(vi) collisions between the traced charged particles with each other and with the atoms of the background gas are checked for and are executed.

Taking as an example electropositive noble gas discharges; elastic scattering, excitation and ionization processes are typically considered for the electrons. For electron–atom collisions the cold gas approximation is commonly used in PIC/MCC simulations. For ions it is usually sufficient to take into account elastic collisions, except at high voltages, where excitation and ionization may as well occur in ion–atom collisions.

Concerning elastic ion–atom collisions, here the recommendation of Phelps [42] is followed: the momentum transfer cross section, Q_m, is split into an isotropic and a backward scattering part, $Q_m = 2Q_b + Q_i$. For a discussion on the relation of the (symmetric) charge exchange cross section and the backward scattering cross section see [42], we only note that at high ion energies these cross sections are equal. A similar approach to treat anisotropic electron–heavy

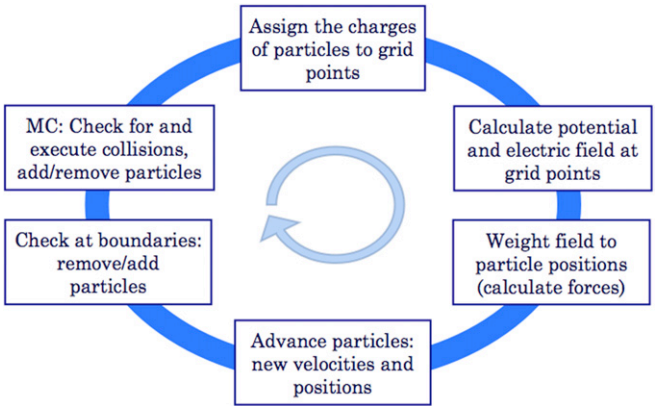

Figure 7. The PIC/MCC cycle for a bounded, collisional plasma.

particle elastic scattering has been developed in [43], and has subsequently been applied in studies of electron [44] and ion [45] transport.

The null-collision method discussed in section 2 is commonly used in PIC/MCC simulations, for both electrons and ions to speed up computations. This avoids the need for checking the collision probability of each particle with the background gas in each time step. Instead of this the number of particles to participate in a collision after a time step Δt (including the option for a null-collision) is obtained as

$$N_{\mathrm{coll}} = N[1 - \exp(-\nu^* \Delta t)], \tag{31}$$

where N is the number of particles of a given kind (electrons or ions).

It is noted that the kinetic properties of the PIC method were found to be negatively affected by inclusion of the collisions [46]. Nonetheless, PIC/MCC simulations provide a detailed insight into the physics of rf plasma sources by delivering spatio-temporal distributions of quantities of interest: particle distribution functions, the ionization and excitation rates, the electron heating rate, as well as the fluxes and densities of different species.

The main practical constraints/requirements for the parameters in PIC/MCC simulations are the following:

(i) the computational grid has to resolve the Debye length, $\Delta x \sim \lambda_{\mathrm{D}}$;
(ii) the time step has to resolve the plasma oscillations of electrons, i.e. $\omega_{\mathrm{p}} \Delta t \leqslant 2$ should hold for stability, where $\omega_{\mathrm{p}} = \sqrt{n_{\mathrm{e,max}} q / \varepsilon_0 m}$ is the electron plasma frequency; in practice, this condition is chosen more restrictively, as $\omega_{\mathrm{p}} \Delta t \leqslant 0.2$;
(iii) the Courant condition must be fulfilled, i.e. we require the particles not to cross a distance greater than the grid division during a time step: $v_{\mathrm{max}} \Delta t \leqslant \Delta x$, in order to have the charges sampled correctly by the grid;
(iv) in order to have a good statistics there should be a reasonably high number ($N_{\mathrm{D}} \gg 1$) of particles present within a Debye sphere;
(v) the collision probability, $1 - \exp(-\nu^* \Delta t)$, should be kept reasonably small, to minimize the probability of more than one collisions of the same particle to take place during Δt.

The above conditions normally require a few hundred to a thousand grid points in one-dimensional simulations of laboratory rf discharges, with typically a few thousand time steps within the rf cycle. As the ions move much more slowly compared with the electrons, a significantly longer time step suffices to move the ions in the discharge. This acceleration technique is known as 'ion subcycling'. The limit imposed by condition (ii) on the time step Δt can be relaxed by using implicit solvers [47, 48].

Fulfilling the Courant condition becomes difficult in discharges operated in the γ-mode (i.e. if the emission of secondary electrons from the electrode surfaces becomes important), especially at higher voltages. In such cases fast electrons (typically those emitted from the electrodes) can be treated as different species and a time step complying with the Courant condition can be used for this relatively small group of electrons, while slow electrons can be moved with a longer time step [49]. As an alternative approach 'event-driven' simulation methods have also been developed [50], which do not suffer from the strict limitation of the time step imposed by the Courant condition on the time-synchronized, classical PIC scheme. For a more detailed comprehensive analysis of the constraints of the PIC/MCC scheme, listed above, the reader is referred to the work of Vahedi *et al* [47].

While early PIC simulations required the use of the most advanced computers, today one-dimensional simulations can be accomplished on PC-class computers, or on small clusters. Calculations in higher dimensions require massive parallel computing, as (i) the solution of the Poisson equation in $D > 1$ is time consuming and (ii) one needs a very high number of superparticles to obtain acceptable statistics.

PIC/MCC simulations have been applied in numerous studies of radiofrequency discharges. In addition to the interest from the theoretical point of view, rf discharges have a variety of applications in several high-tech areas of industry [51]. The most important application fields include etching and deposition processes in chip and solar cell manufacturing, as well as the creation of biocompatible surfaces. These applications are rather demanding and require tailoring of the discharge characteristics to optimize the plasma–surface interaction processes. As most of the processes are driven by ions, the control of ion properties is a key issue. The need for the possibility of a separate control of the ion flux and energy at the wafer's surface has motivated the development of different types of plasma sources and excitation schemes: capacitive discharges operated at multiple frequencies, as well as hybrid (dc–rf, and capacitive–inductive) sources [52–54].

Considering capacitive discharges, sources driven by two different frequencies have been studied extensively during the last decade. The 'classical' types of dual-frequency (df) discharges operate at substantially different frequencies [55–67], where the high-frequency voltage (V_{HF}) is supposed to control the plasma density and consequently the ion flux, whereas the low-frequency voltage ($V_{\mathrm{LF}} > V_{\mathrm{HF}}$) is responsible for accelerating the ions through the sheath, i.e. for controlling the ion energy. In reality, the independent control of ion properties using this approach is limited, as will be explained later. A new approach, based on the 'electrical

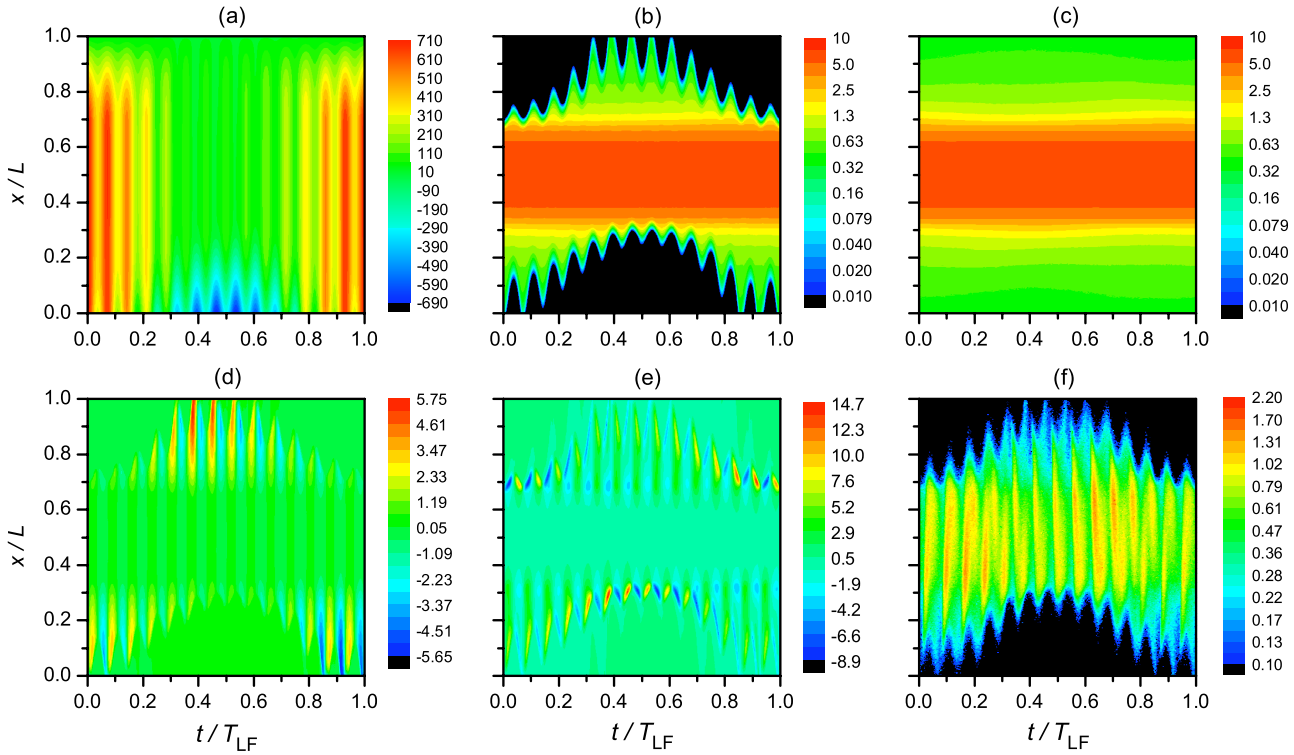

Figure 8. Spatio-temporal distributions of different discharge characteristics obtained from a 1D PIC/MCC simulation of a dual-frequency rf discharge in argon, at 6.6 Pa pressure, $L = 2.5$ cm, $V_{HF} = 200$ V, $f_{HF} = 27.12$ MHz, $V_{LF} = 500$ V, $f_{LF} = 1.937$ MHz and $\gamma = 0.1$. (*a*) Potential (V), (*b*) electron density (10^{15} m^{-3}), (*c*) ion density (10^{15} m^{-3}), (*d*) electron velocity (10^5 m s^{-1}), (*e*) electron power absorption (10^4 W m^{-3}) and (*f*) total excitation rate (10^{21} m^{-3} s^{-1}). The powered electrode is situated at the bottom, $x = 0$, while the electrode at $x/L = 1$ is grounded. T_{LF} is the period of the low-frequency (1.937 MHz) cycle.

asymmetry effect' utilizes a fundamental frequency and its second harmonic with fixed, but adjustable phase shift for a nearly independent control of ion properties [68–72]. The examples shown here relate to these two types of df discharges. The simulations are carried out for argon discharges, and the cross sections of the collision processes are taken from [12, 42, 73].

Figure 8 illustrates the results of a 1D PIC/MCC simulation of a dual-frequency rf discharge. The powered electrode is driven with a voltage waveform:

$$V(t) = V_{HF}\cos(2\pi f_{HF}t) + V_{LF}\cos(2\pi f_{LF}t). \qquad (32)$$

The simulations have been carried out for a pressure of $p = 6.6$ Pa and an electrode gap $L = 2.5$ cm. The high-frequency ('HF') voltage is 200 V, $f_{HF} = 27.12$ MHz, the low-frequency ('LF') voltage is 500 V, $f_{LF} = 27.12/14$ MHz $\cong 1.937$ MHz. The secondary electron yield is $\gamma = 0.1$. The spatio-temporal behavior of the quantities shown in figure 8 reveals details of the discharge operation. The potential and electron density distribution (panels (*a*) and (*b*)) reflect the details of the sheath dynamics. The electron density follows the variation of the potential, while the ion density profile is stationary. The complicated patterns of electron velocity (panel (*d*)) and of electron heating/cooling (panel (*e*)) provide insight into the electron dynamics. The sheath expansion results in the formation of energetic beams of electrons [74], which is clearly shown in the map of the total electron impact excitation rate, as seen in panel (*f*). These beams are strongest during the expansion phases of the high-frequency sheath during the times of low-frequency sheath collapse. This coupling of the frequencies [62, 63, 66, 75] results in an interdependence between the ion flux and energy, limiting their separate control.

Finally, we analyze some properties of a discharge that operates under the conditions of the electrical asymmetry effect (EAE). As already mentioned above, the EAE [68–72] in geometrically symmetric discharge arrangements can be realized by driving the discharge with two frequencies: a base frequency f and its second harmonic $2f$. Control of the locked, but adjustable phase angle, θ, between the two sources results in the development of a variable dc self-bias, η. The fact that the bias can be tuned over a wide range by changing θ gives a possibility for a nearly independent control of the ion flux and ion energy at the electrodes. This way the EAE solves the problem of frequency coupling in classical dual-frequency discharges. Figure 9 displays the results of a PIC/MCC simulation for the spatio-temporal distribution of the ionization rate and the VDFs of the electrons. The discharge is excited by a voltage wave form:

$$V(t) = V_0[\cos(\omega t + \theta) + \cos(2\omega t)], \qquad (33)$$

at $p = 5$ Pa, $L = 2.5$ cm, $V_0 = 500$ V. For the present case $\theta = 0°$ is chosen, which results in a dc self-bias of $\eta = -370$ V.

The central panel of figure 9 shows the spatio-temporal distribution of the ionization rate in the discharge in the form of a color map. Equipotential surfaces, separated by a difference of 20 V, emphasizing the development of sheath regions are superimposed. The ionization rate exhibits a strong maximum,

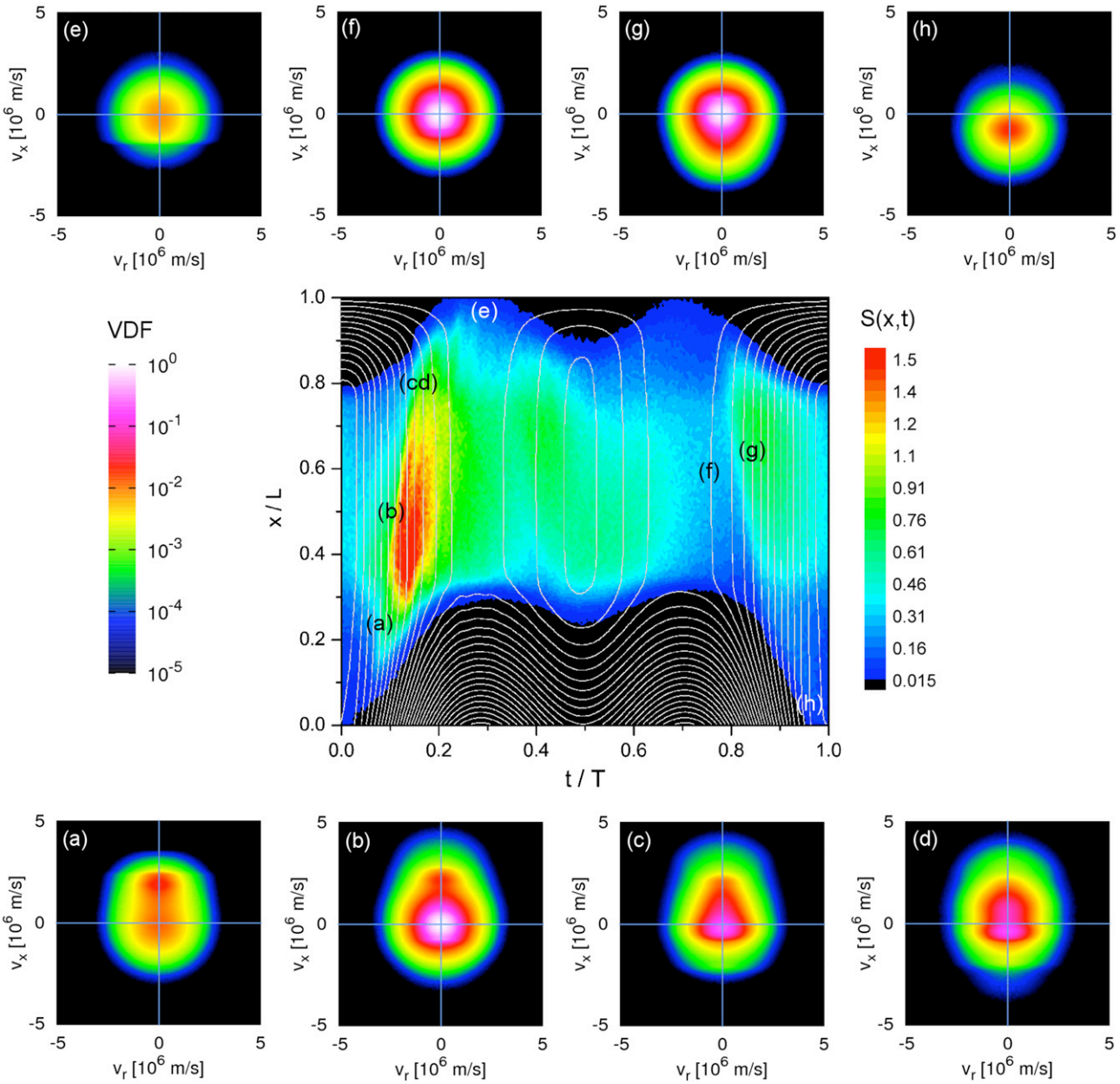

Figure 9. Central panel: spatio-temporal distribution of the ionization rate in a dual-frequency argon rf discharge driven by a voltage waveform defined by equation (33), at 13.56 MHz and 27.12 MHz, $V_0 = 500$ V, $\theta = 0°$, $p = 5$ Pa, $L = 2.5$ cm. The coordinate x is measured from the powered electrode, T is the period of the 13.56 MHz signal. The color scale of the ionization rate, $S(x, t)$ (given in units of 10^{21} m^{-3} s^{-1}), is logarithmic and covers two orders of magnitude. Superimposed on the plot are equipotential lines; their distance is 20 V. (*a*)–(*h*) velocity distribution functions of electrons at positions and times indicated in the central panel. The color scale of the VDFs is logarithmic and covers five orders of magnitude. An interactive version of this figure is available online [77].

related to the formation of an energetic beam of electrons at the rapid sheath expansion at the powered electrode [74]. The formation of this beam can clearly be seen in panels (*a*) and (*b*), where we observe a strong component in the VDF propagating into the positive x direction (upwards in the plots). The spatial and temporal positions corresponding to the panels showing the VDFs are identified in the central panel of figure 9. This beam, propagating toward the grounded (upper) electrode reaches the grounded sheath during the phase of sheath collapse—see panel (*d*). The sheath is, however, not yet fully collapsed at this time, and we can observe here a reflection of fast electrons [74]—while the VDF shown in panel (*d*) still shows significant upward propagation, a weak downward propagating component can also be observed. At the collapse of the grounded sheath an asymmetry of the VDF (see panel (*e*)) similar to that observed near the absorbing anode in a Townsend discharge is seen (cf figure 3). At the position corresponding to panel (*e*) there are a few volts potential with respect to ground, and the electrons, which are able to overcome this potential difference, reach the grounded electrode and are absorbed with a high probability. The electrons with lower v_x velocity are reflected from the potential barrier and as a result of these two effects the downward propagating electron population is depleted at higher velocity.

Additional weaker electron beams are also launched from the grounded sheath upon sheath expansions, at about $t/T = 0.4$ and 0.8, as seen in the central panel. Panel (f) shows an isotropic VDF in the bulk plasma, at a time when electron beams are absent. Panel (g) shows a weaker, downward propagating electron population induced by the sheath expansion at the grounded (upper) electrode. Finally, panel (h) shows a nearly isotropic VDF in the vicinity of the powered (lower) electrode at the phase of rapid sheath retraction. Here the entire VDF is shifted into the negative x direction, indicating that an electric field reversal is present in this region to accelerate electrons that cannot follow the collapsing sheath [76]. This local effect is very much different from the situation depicted in figures 9(a) and (b), where the formation of beams is a non-local phenomenon, affecting only a small part of the electron population.

In this simulation the VDFs have been acquired at 50×50 positions in space and time; an interactive version of this figure, allowing us to observe all these VDFs, is available online [77].

6. Summary

This paper aimed to outline the basics of particle simulation methods applicable for studies of low-pressure discharges: Townsend discharges, abnormal glow discharges, as well as capacitive radiofrequency discharges. These methods enable tracing of the particles at the kinetic level under the highly non-equilibrium behavior of these discharges. They provide direct access to the velocity distribution function of the particles, which contains the full information about the ensemble of the particles, with spatial and temporal resolution.

Illustrative examples were given for the kinetics of electrons in homogeneous electric fields, both for stationary conditions and for the case of spatio-temporal relaxation. The usefulness of the Monte Carlo method, coupled to a fluid description of cold-cathode dc glow discharges has been demonstrated. The spatio-temporal behavior of the discharge characteristics and the electron VDF were calculated using a PIC/MCC simulation of dual-frequency rf discharges.

Thanks to the continuous rapid advance of computational resources, particle-based methods are expected to play an increasingly important role in simulations of various kinds of plasmas.

Acknowledgments

This paper is based on the W Crookes Prize lecture at the 20th ESCAMPIG. The author thanks his numerous collaborators and the Hungarian Scientific Research Fund (OTKA, current grant K77653) for having supported his work for 20 years. The help of Aranka Derzsi (computing the data appearing in figure 5) and Julian Schulze (critical reading and correcting the manuscript) is gratefully acknowledged.

References

[1] Robson R E, White R D and Petrović Z Lj 2005 *Rev. Mod. Phys.* **77** 1303
Pitchford L C, Boeuf J-P, Segur P and Marode E 1990 *Non-equilibrium Effects in Ion and Electron Transport* ed J W Gallagher (New York: Plenum)
Tsendin L D 1995 *Plasma Sources Sci. Technol.* **4** 200
Tsendin L D 2009 *Plasma Sources Sci. Technol.* **18** 014020
Kudryavtsev A A, Morin A V and Tsendin L D 2008 *Tech. Phys.* **53** 1029
[2] Tsendin L D 2010 *Phys.—Usp.* **53** 133
[3] Pitchford L C, ONeil S V and Rumble J R Jr 1981 *Phys. Rev.* A **23** 294
Robson R E and Ness K F 1986 *Phys. Rev.* A **33** 2068
Richley E 1999 *Phys. Rev.* E **59** 4533
Loffhagen D and Sigeneger F 2009 *Plasma Sources Sci. Technol.* **18** 034006
Dujko S and White R D 2008 *J. Phys.: Conf. Ser.* **133** 012005
Dujko S, White R D, Petrović Z Lj and Robson R E 2010 *Phys. Rev.* E **81** 046403
Winkler R, Arndt S, Loffhagen D, Sigeneger F and Uhrlandt D 2004 *Contrib. Plasma Phys.* **44** 437
Kolobov V I and Arslanbekov R R 2006 *IEEE Trans. Plasma Sci.* **34** 895
Petrović Z Lj, Raspopović Z M, Dujko S and Makabe T 2002 *Appl. Surf. Sci.* **192** 1
[4] Nanbu K 2000 *IEEE Trans. Plasma Sci.* **28** 971
[5] Longo S 2000 *Plasma Sources Sci. Technol.* **9** 468
[6] An Tran Ngoc, Marode E and Johnson P C 1977 *J. Phys. D: Appl. Phys.* **10** 2317
Boeuf J P and Marode E 1984 *J. Phys. D: Appl. Phys.* **17** 1133
Braglia G L and Romano L 1984 *Lett. Nuovo Cimento* **40** 513
Stojanovic V D and Petrović Z Lj 1998 *J. Phys. D: Appl. Phys.* **31** 834
Lawler J E and Kortshagen U 1999 *J. Phys. D: Appl. Phys* **32** 3188
Dujko S, Raspopović Z M and Petrović Z Lj 2005 *J. Phys. D: Appl. Phys.* **38** 2952
Donkó Z, Rózsa K and Tobin R C 1996 *J. Phys. D: Appl. Phys.* **29** 105
Longo S 2006 *Plasma Sources Sci. Technol.* **15** S181
[7] Hendricks J S 1994 *Los Alamos Sci.* **22** 30
[8] Ding Li, Sudakov M and Kumashiro S 2002 *Int. J. Mass. Spectrom.* **221** 117
[9] Yousfi M, Hennad A and Alkaa A 1994 *Phys. Rev.* E **49** 3264
[10] Okhrimovskyy A, Bogaerts A and Gijbels R 2002 *Phys. Rev.* E **65** 037402
[11] Opal C B, Peterson W K and Beaty E C 1971 *J. Chem. Phys.* **55** 4100
[12] Phelps A V, unpublished http://jila.colorado.edu/~avp/collision_data/
[13] Skullerud H R 1968 *J. Phys. D: Appl. Phys.* **1** 1567
[14] http://plasma.szfki.kfki.hu/~zoli/research/avalanche
[15] Lin S L and Bardsley J N 1977 *J. Chem. Phys* **66** 435
[16] Weng Y and Kushner M J 1990 *Phys. Rev.* A **42** 6192
[17] Li Y M, Pitchford L C and Moratz T J 1989 *Appl. Phys. Lett.* **54** 1403
[18] Tagashira H 1992 *Aust. J. Phys.* **45** 365
Petrović Z Lj, Dujko S, Marić D, Malović G, Nikitović Ž, Šašić O, Jovanović J, Stojanović V and Radmilović-Radjenović M 2009 *J. Phys. D: Appl. Phys.* **42** 194002
Morgan W L 1991 *Phys. Rev.* A **44** 1677
Pinhão N R, Donkó Z, Loffhagen D, Pinheiro M and Richley E A 2004 *Plasma Sources Sci. Technol.* **13** 719
[19] Malović G, Strinić A, Živanov A, Marić D and Petrović Z Lj 2003 *Plasma Sources Sci. Technol.* **12** S1
[20] Loffhagen D, Winkler R and Donkó Z 2002 *Eur. Phys. J. Appl. Phys.* **18** 189
[21] Phelps A V 2001 *Plasma Sources Sci. Technol.* **10** 329
[22] Kim H C, Iza F, Yang S S, Radmilović-Radjenović M and Lee J K 2005 *J. Phys. D: Appl. Phys.* **38** R283

[23] Becker M M, Loffhagen D and Schmidt W 2009 *Comput. Phys. Commun.* **180** 1230
[24] Surendra M, Graves D B and Jellum G M 1990 *Phys. Rev.* A **41** 1112
Boeuf J-P and Pitchford L C 1991 *IEEE Trans. Plasma Sci.* **19** 286
Bogaerts A, Gijbels R and Goedheer W J 1996 *Anal. Chem.* **68** 2296
Donkó Z 2001 *Phys. Rev.* E **64** 026401
Brok W J M, Wagenaars E, van Dijk J and van der Mullen J J A 2007 *IEEE Trans. Plasma Sci.* **35** 1325
[25] Bouef J-P and Pitchford L C 1995 *J. Phys. D: Appl. Phys.* **28** 2083
[26] Derzsi A, Hartmann P, Korolov I, Karácsony J, Bánó G and Donkó Z 2009 *J. Phys. D: Appl. Phys.* **42** 225204
[27] Donkó Z, Hartmann P and Kutasi 2006 *Plasma Sources Sci. Technol.* **15** 178
[28] Revel I, Pitchford L C and Bouef J-P 2000 *J. Appl. Phys.* **88** 2234
Donkó Z 2000 *J. Appl. Phys.* **88** 2226
Bogaerts A and Gijbels R 1997 *Spectrochim. Acta* **B52** 765
Marić D, Hartmann P, Malović G, Donkó Z and Petrović Z Lj 2003 *J. Phys. D: Appl. Phys.* **36** 2639
Kutasi K and Donkó Z 2000 *J. Phys. D: Appl. Phys.* **33** 1081
Callegari Th, Ganter R and Boeuf J-P 2000 *J. Appl. Phys.* **88** 3905
Bogaerts A and Gijbels R 1998 *Spectrochim. Acta* **B53** 437
Boeuf J-P and Garrigues L 1998 *J. Appl. Phys.* **84** 3541
[29] Hagelaar G J M and Pitchford L 2005 *Plasma Sources Sci. Technol.* **14** 722
[30] Grubert G K, Becker M M and Loffhagen D 2009 *Phys. Rev.* E **80** 036405
[31] Pinheiro M J 2004 *Phys. Rev.* E **70** 056409
[32] Bánó G, Hartmann P, Kutasi K, Horváth P, Plašil R, Hlavenka P, Glosík J and Donkó Z 2007 *Plasma Sources Sci. Technol.* **16** 492
[33] Rózsa K, Gallagher A and Donkó Z 1995 *Phys. Rev.* E **52** 913
Marić D, Kutasi K, Malović G, Donkó and Petrović Z Lj 2002 *Eur. Phys. J.* D **21** 73
[34] Boeuf J P and Marode E 1982 *J. Phys. D: Appl. Phys.* **15** 2169
[35] Birdsall C K and Langdon A B 1985 *Plasma Physics via Computer Simulation* (New York: McGraw-Hill)
[36] Hockney R W and Eastwood J W 1981 *Computer Simulation Using Particles* (New York: McGraw-Hill)
[37] Lieberman M A, Booth J P, Chabert P, Rax J M and Turner M M 2002 *Plasma Sources Sci. Technol.* **11** 283
Chabert P 2007 *J. Phys. D: Appl. Phys.* **40** R63
[38] Birdsall C K 1991 *IEEE Trans. Plasma Sci.* **19** 65
[39] Verboncoeur J P 2005 *Plasma Phys. Control. Fusion* **47** A231
[40] Matyash K, Schneider R, Taccogna F, Hatayama A, Longo S, Capitelli M, Tskhakaya D and Bronold F X 2007 *Contrib. Plasma Phys.* **47** 595
[41] Tskhakaya D, Matyash K, Schneider R and Taccogna F 2007 *Contrib. Plasma Phys.* **47** 563
[42] Phelps A V 1994 *J. Appl. Phys.* **76** 747
[43] Longo S and Capitelli M 1994 *Plasma Chem. Plasma Proc.* **14** 1
[44] Biagi S F 1999 *Nucl. Instrum. Methods Phys. Res.* A **421** 234
[45] Trunec D 1995 *Int. J. Mass Spectrom. Ion Proc.* **149/150** 179
[46] Turner M M 2006 *Phys. Plasmas* **13** 033506
[47] Vahedi V, DiPeso G, Birdsall C K, Lieberman M A and Rognlien T D 1993 *Plasma Sources Sci. Technol.* **2** 261
[48] Cohen B I, Langdon A B and Friedman A 1982 *J. Comput. Phys.* **46** 15
[49] Donkó Z, Schulze J, Hartmann P, Korolov I, Czarnetzki U and Schüngel E 2010 *Appl. Phys. Lett.* **97** 081501
[50] Omelchenko Y A and Karimabadi H 2006 *J. Comput. Phys.* **216** 153
[51] Lieberman M A and Lichtenberg A J 2005 *Principles of Plasma Discharges and Materials Processing* 2nd edn (New York: Wiley-Interscience)
[52] Jiang W, Xu X, Dai Z-L and Wang Y-N 2008 *Phys. Plasmas* **15** 033502
Kawamura E, Lichtenberg A J and Lieberman M A 2008 *Plasma Sources Sci. Technol.* **17** 045002
[53] Wang S-B and Wendt A E 2000 *J. Appl. Phys.* **88** 643
[54] Rauf S and Kushner M J 1999 *IEEE Trans. Plasma Sci.* **27** 1329
Dudin S V, Zykov A V, Polozhii K I and Farenik V I 1998 *Tech. Phys. Lett.* **24** 881
[55] Georgieva V and Bogaerts A 2006 *Plasma Sources Sci. Technol.* **15** 368
[56] Bojarov A, Radmilović-Radjenović M and Petrović Z Lj 2008 *Publ. Astron. Obs. Belgrade* **84** 387
[57] Lee S H, Tiwari P K and Lee J K 2009 *Plasma Sources Sci. Technol.* **18** 025024
[58] Lisovskiy V, Booth J P, Landry K, Douai D, Cassagne V and Yegorenkov V 2008 *Plasma Sources Sci. Technol.* **17** 025002
[59] Olevanov M, Proshina O, Rakhimova T and Voloshin D 2008 *Phys. Rev.* E **78** 026404
[60] Mussenbrock T, Ziegler D and Brinkmann R P 2006 *Phys. Plasmas* **13** 083501
[61] Kawamura E, Lieberman M A and Lichtenberg A J 2006 *Phys. Plasmas* **13** 053506
[62] Gans T, Schulze J, O'Connell D, Czarnetzki U, Faulkner R, Ellingboe A R and Turner M M 2006 *Appl. Phys. Lett.* **89** 261502
[63] Schulze J, Gans T, O'Connell D, Czarnetzki U, Ellingboe A R and Turner M M 2007 *J. Phys. D: Appl. Phys.* **40** 7008
[64] Boyle P C, Ellingboe A R and Turner M M 2004 *Plasma Sources Sci. Technol.* **13** 493
[65] Waskoenig J and Gans T 2010 *Appl. Phys. Lett.* **96** 181501
[66] Schulze J, Donkó Z, Luggenhölscher D and Czarnetzki U 2009 *Plasma Sources Sci. Technol.* **18** 034011
[67] Voloshin D, Proshina O and Rakhimova T 2010 *J. Phys. Conf. Series* **207** 012026
[68] Heil B G, Schulze J, Mussenbrock T, Brinkmann R P and Czarnetzki U 2008 *IEEE Trans. Plasma Sci.* **36** 1404
[69] Heil B G, Czarnetzki U, Brinkmann R P and Mussenbrock T 2008 *J. Phys. D: Appl. Phys.* **41** 165202
[70] Donkó Z, Schulze J, Heil B G and Czarnetzki U 2009 *J. Phys. D: Appl. Phys.* **42** 025205
[71] Schulze J, Schüngel E, Donkó Z and Czarnetzki U 2010 *J. Phys. D: Appl. Phys.* **43** 225201
Schulze J, Schüngel E, Donkó Z and Czarnetzki U 2010 *Plasma Sources Sci. Technol.* **19** 045028
[72] Wang Y-N, Jiang W and Hou L-J 2010 *J. Appl. Phys.* in press
[73] Phelps A V and Petrović Z Lj 1999 *Plasma Sources Sci. Technol.* **8** R21
[74] Schulze J, Heil B G, Luggenhölscher D, Mussenbrock T, Brinkmann P R and Czarnetzki U 2008 *J. Phys. D: Appl. Phys.* **41** 042003
Schulze J, Heil B G, Luggenhölscher D, Brinkmann R P and Czarnetzki U 2008 *J. Phys. D: Appl. Phys.* **41** 195212
Schulze J, Heil B G, Luggenhölscher D and Czarnetzki U 2008 *IEEE Trans. Plasma Sci.* **36** 1400
[75] Turner M M and Chabert P 2006 *Phys. Rev. Lett.* **96** 205001
[76] Schulze J, Donkó Z, Heil B G, Luggenhölscher D, Mussenbrock T, Brinkmann R P and Czarnetzki U 2008 *J. Phys. D: Appl. Phys.* **41** 105213
[77] http://plasma.szfki.kfki.hu/~zoli/research/rf1